Image-based Numerical Modeling of Self-Healing in a Ceramic-Matrix Minicomposite

Grégory Perrot, Guillaume Couégnat, Mario Ricchiuto, Gérard Vignoles

Image-based Numerical Modeling of Self-Healing in a Ceramic-Matrix Minicomposite

Grégory Perrot[a,b], Guillaume Couégnat[c], Mario Ricchiuto[b], Gerard L. Vignoles[a]

[a] *University of Bordeaux,*
Laboratoire des Composites ThermoStructuraux (LCTS)
UMR 5801: CNRS-Safran-CEA-UBx
3, Allée de La Boétie, 33600 Pessac, France
Tel: (+33) 5 5684 4700
[b] *Team CARDAMOM, Inria Bordeaux Sud-Ouest*
200 Avenue de la vieille tour
33405 Talence cedex
[c] *CNRS, Laboratoire des Composites ThermoStructuraux (LCTS)*

Abstract

Self-healing is an important phenomenon in new-generation refractory ceramic-matrix composites, obtained by the oxidation of a glass-forming phase in the composite. The dynamics of oxygen diffusion, glass formation and flow are the basic ingredients of a self-healing model that has been developed here in 2D in a transverse crack of a minicomposite. The presented model can work on a realistic image of the material section and is able to simulate healing and quantify the exposure of the material to oxygen, a prerequisite for its lifetime prediction. Crack reopening events are handled satisfactorily, and secondary healing can be simulated. This papers describes and discusses a typical case in order to show the model potentialities.

Keywords:

Highlights

- Numerical model features oxidation kinetics and liquid oxide flow

Email address: vinhola@lcts.u-bordeaux.fr (Gerard L. Vignoles)

- Model works on material images or on virtual material meshes (incorporates realistic fiber arrangements and size distributions)
- Describes self-healing restart after crack reopening

1. Introduction

Self-healing Ceramic-Matrix Composites (SH-CMCs) are very promising materials for use as civil aircraft jet engine hot parts [1]. Tests in true conditions of use have been carried out, showing excellent lifetimes [2]. These materials are constituted of a 3D woven arrangement of SiC fiber tows, infiltrated by an interphase and a multilayer matrix, all of them having a specific function. The pyrocarbon (pyC) interphase acts as a crack deviator and prevents premature fiber failure while the matrix undergoes multiple cracking, that is, progressive damage [3]. In addition, SiC matrix layers bring stiffness and are chemically inert at moderate temperatures. Finally, boron-containing phases produce a liquid oxide which fills cracks above 450°C and prevents further oxidation by a diffusion barrier effect [4]. This increases by large amounts the material lifetime under exposition to high-temperature oxidation [5]. The massive production of SH-CMC parts in engines can only be foreseen if there is a sufficient confidence in the material lifetime duration. The trouble is that the material can last as long as ten years; hence, a material development cycle based only on experimental characterization is not feasible. Modelling is mandatory in order to incorporate as much understanding of the material's physics as possible, and identify and explain the experiments that have been carried out in "accelerated degradation" conditions, or on material parts. The present work has been developed in this frame.

The lifetime of SH-CMCs results from a balance between degradation and self-healing [6]. The network of matrix cracks brings the oxygen in contact with all the inner material constituents; they are transformed gradually into oxides,

some of them being gaseous (e.g. carbon), liquid (e.g. boron) or solid (e.g. silica at moderate temperatures). The calculation of the chemical reaction rate everywhere in the material is a key point for lifetime prediction. Past reports have described models which give the time evolution of the oxygen concentration in, say, some key part of the composite (*i.e.* the weakest, most exposed fiber); they deduce from this quantity a global lifetime because the tensile strength of this fiber can be related to oxygen exposure through an oxygen-dependent slow crack growth rate law [7, 8]. These models were developed in 0 [9, 10] or 1 [11] space dimension.

In reality, the materials have a complex structure, as illustrated in figure 1. SiC filament bundles are woven in a 3D interlocking pattern. Then, the multi-layered matrix is deposited – usually by Chemical Vapor Infiltration (CVI) – around the fiber, with varying thicknesses depending on the location : large close to the part boundaries, and small inside the fiber bundles. Pores and cracks are distributed unevenly throughout the material. Accordingly, it appears interesting to design modeling tools that may address the material complexity and multi-scale organization.

Here, in order to bridge descriptions of the self-healing phenomenon between fiber and tow scales (figures 1*c* and *d*), we propose an image-based approach, in which the resolution domain is a 2D Finite Element (FE) mesh directly obtained from home-made mesh generation software.

The paper is organized as follows. First, the model is set up and translate into equations. Then, the employed numerical schemes are described and their validation is discussed. Then, an application example is presented in detail, in order to give an idea of the potential of the modelling toolbox.

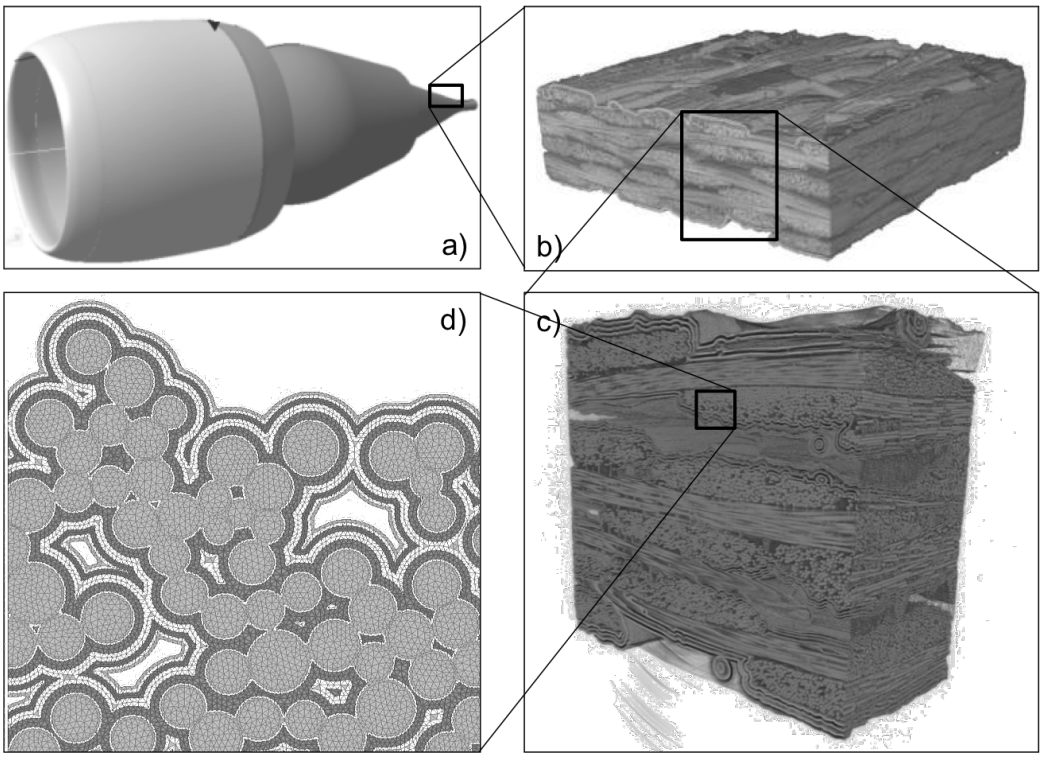

Figure 1: Successive close-ups of a self-healing Ceramic-Matrix Composite in an aerospace propulsion device. a) Engine and part scale (computer-aided sketch); b) Weaving scale (X-ray CMT scan); c) Tow scale (X-ray CMT scan); d) Fiber scale (FE mesh).

2. Model setup

Though the material has a multi-scale character, we will focus here only on mini-composites, that is, straight bundles of filaments with multilayer coatings. The concept of mini-composite has been thoroughly used in order to build up a comprehension of how a full composite works [12], but with a simplified mechanical stress state. Models addressing mini-composites usually take advantage of the separation of the space coordinates into longitudinal (z) and transverse (x, y), allowing for 1D models after homogenizing on a transverse section.

As far as CMCs are concerned, one of the most important mechanical test configurations is tensile stress along the fibers, since it leads to matrix crack opening and eventually to material failure. This will be the situation considered here.

2.1. Material description

The transverse section of a typical SH-CMC minicomposite model is depicted on fig. 1d. Several domains are easily recognized:

1. The SiC fibers, which are sensitive to oxidation through a subcritical crack growth behavior. Their diameter is in the range 8-15 μm.
2. The thin pyrocarbon (PyC) interphase coating the fibers. This layer acts a crack deviator, helping the development of multi-cracking, which gives the material its exceptional mechanical behavior [3, 13].
3. The multi-layer matrix containing two constituents: silicon carbide, which is nearly inert at the temperatures typical of civil aircraft applications (it begins to oxidize appreciably above 1000°C [14]), and boron carbide, yielding a liquid (glassy) phase upon oxidation [4, 5].
4. A number of cusp-shaped pores left by the production process. In particular, the PyC, SiC and boron carbide layers are deposited by Chemical Vapor

Infiltration (CVI) [15, 16]. This process gives characteristic continuous layers growing in conformal shape with respect to the initial substrate (*i.e.* the fibers). The layer thicknesses are larger in the outer parts of the fiber bundles, because of the competition between chemical deposition reactions and gas diffusion [17]. As a result, some pores remain between the fibers after infiltration. These imperfections may be connected or not to the ambient atmosphere, depending on whether the crack network intercepts them.

2.2. Phenomena and scales

Under tensile stress, the mini-composite will undergo matrix transverse multicracking [18, 19]. In this case, cracks are mostly perpendicular to the fiber direction [20]. Some may exhibit a helicoidal structure [21], but the helix vertical spacing is much larger than the crack thickness. We can thus safely focus on transversal cracks and adjust any micro-mechanical model to the measured behavior through the value of the average spacing between two successive cracks. The thickness of the cracks is of the order of less than 1 μm, *i.e.* 10^{-3}-10^{-2} times the typical diameter of the mini-composite [20]. Even in presence of these cracks, fibers continue to provide the material with mechanical continuity, and tensile resistance [18]. Nevertheless, the cracks provide a path to oxidizing species toward the fibers [22, 23]. This constitues the root of the weakening of the fibers themselves, and thus of the failure of the material [24, 25].

The key phenomenon controlling the material lifetime is oxidation [26]. The most sensitive component is the pyrocarbon coating which undergoes active oxidation above 500°C [27]. At temperatures between 450°C and about 700°C, typical of civil craft engine operating conditions, the oxidation of the boron carbide matrix component is efficient enough to fill active cracks with a liquid boron oxide [28]. This is caused by the higher molar volume of the oxide as compared to the carbide. At low enough temperatures, the flow of this liquid is dominated by vis-

cous effects, with respect to which both inertial and capillary effects are negligible [26]. The oxide is thus pushed through the crack by its own growth. Oxygen diffusion through the oxide is considerably slower than in the gas phase. Typically, the time scale of the diffusion through the liquid is 10^5 times larger than that into the gas [29]. Silicon carbide may also produce a solid silica layer upon oxidation [30]; however, the temperatures considered here ($< 650°C$) are not high enough to allow the development of a significant silica thickness [31].

2.3. Problem equations

The natural ingredients of the model are the concentration balance for gaseous oxygen, and for all oxidized materials, namely, pyrocarbon, undergoing active oxidation and giving gaseous CO_2

$$C(s) + O_2(g) \longrightarrow CO_2(g), \tag{1}$$

and boron carbide, yielding a liquid B_2O_3 oxide together with dissolved, then gaseous CO_2 [32]

$$B_4C_{1.6}(s) + 4.6\ O_2(g) \longrightarrow 2\ B_2O_3(l) + 1.6\ CO_2(g). \tag{2}$$

Note the stoichiometry of boron carbide, experimentally determined as in excess carbon with respect to the known B_4C or $B_{13}C_2$ formulæ. Transport equations for oxygen mass and for the liquid oxide mass are established by resorting to an asymptotic, crack-averaged, two-dimensional description. We exploit the fact that the ratio of the crack thickness e over the mini-composite diameter d is small. As recalled in section §2.2, this ratio assumes in practice values $\epsilon = e/d \in [10^{-3}, 10^{-2}]$. In our approach, the three-dimensional governing equations, *e.g.* Fick's law for oxygen concentration, are integrated over the crack thickness, and higher order variations (in ϵ), are neglected. This procedure has two effects:

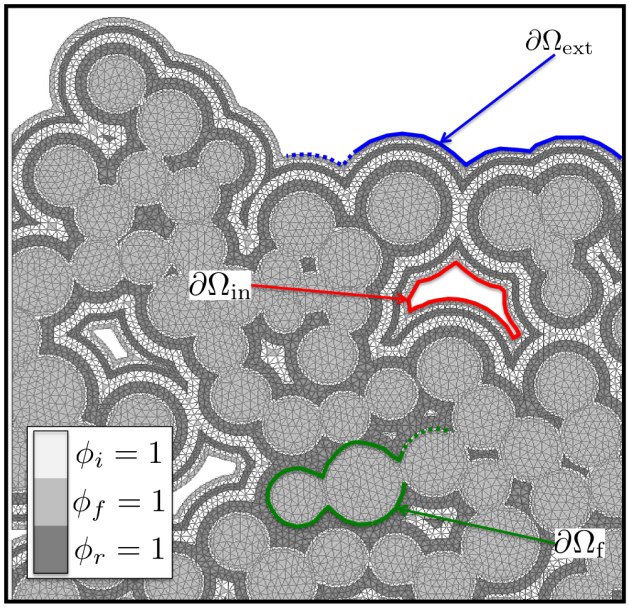

Figure 2: Definition of the computational regions

- (*i*) the model provides only an averaged two-dimensional description of the transport processes within the crack. The main unknowns are the local crack averaged values of the O_2 concentration and of the oxide flow velocity, and the local height of liquid oxide within the crack ;

- (*ii*) mass fluxes associated to chemical reactions, normally appearing in three dimensions as boundary conditions on the upper/lower crack boundaries, are embedded in the equations as source terms which arise naturally from the integration procedure.

The obtained model is defined on a domain decomposed in several sub-domains and boundaries, as illustrated in figure 2:

- Ω_r: reactive regions of the matrix (indicated by $\phi_r(\mathbf{r}) = 1$ if $\mathbf{r} \in \Omega_r$, 0 elsewhere),

- Ω_i: inert regions (indicated similarly by $\phi_i(\mathbf{r})$),

- Ω_f: fibers (indicated similarly by $\phi_f(\mathbf{r})$),
- $\partial\Omega_{\text{ext}}$: the external boundary ,
- $\partial\Omega_{\text{in}}$: the internal boundaries delimiting macro-pores, and
- $\partial\Omega_{\text{f}}$: the fibers boundaries .

The balance equation for the oxygen evolution, defined on the reactive and inert domains, reads as follows

$$\partial_t(hC_{\mathrm{O}_2}) + \nabla \cdot \mathbf{F}_{\mathrm{O}_2} = S_{\mathrm{O}_2} \tag{3}$$

where the effective height h available to oxygen transfer is computed as

$$h = \phi_l e(x, y) + \phi_g h_g \,, \qquad \phi_l + \phi_g = 1 \tag{4}$$

where the phase indicators $\phi_l(x, y)$ and $\phi_g(x, y)$ take the values 1 or 0 depending on whether the considered point is in a region occupied by the liquid plug ($\phi_l = 1$) or not. The quantity $e(x, y)$ denotes the local thickness of the crack, and the values of h_l and h_g are determined by both chemical reactions and oxide flow, as we will shortly see. The crack height-averaged oxygen flux $\mathbf{F}_{\mathrm{O}_2}$ is given by

$$\mathbf{F}_{\mathrm{O}_2} = -(\phi_l e(x, y)\mathcal{D}_l + \phi_g h_g \mathcal{D}_g)\nabla C_{\mathrm{O}_2} \,, \tag{5}$$

with $\mathcal{D}_l$ and $\mathcal{D}_g$ the oxygen diffusion coefficients in the liquid and gas phases, respectively, and with oxygen consumption driven by the (algebraic) source term

$$S_{\mathrm{O}_2} = -\phi_r \frac{k_l}{4.6} C_{\mathrm{O}_2} \tag{6}$$

with an effective reaction rate k_l defined using the Deal-Grove model [33] as:

$$\frac{1}{k_l} = \frac{1}{k_{\mathrm{B_2O_3}}} + \frac{h_l - e}{\mathcal{D}_l} \,. \tag{7}$$

Here, the liquid-phase diffusion coefficient $\mathcal{D}_l$ is related to the parabolic kinetic constant of oxidation. The evolution equation for the liquid height h_l, without flow, is an ordinary differential equation :

$$\frac{dh_l}{dt} = -2V_{m,\mathrm{B_2O_3}} S_{\mathrm{O_2}} \tag{8}$$

Simultaneously, the height of available boron carbide decreases according to the following equation:

$$\frac{dh_{\mathrm{B}_x\mathrm{C}}}{dt} = V_{m,\mathrm{B}_x\mathrm{C}} S_{\mathrm{O_2}} \tag{9}$$

As a result, the available height for gas circulation above the liquid in the reactive zone obeys:

$$\frac{dh_g}{dt} = \left(2V_{m,\mathrm{B_2O_3}} - V_{m,\mathrm{B}_x\mathrm{C}}\right) S_{\mathrm{O_2}} \tag{10}$$

The pyrocarbon consumed height obeys to the following equation:

$$\frac{dh_p}{dt} = V_{m,\mathrm{C}} k_p C_{\mathrm{O_2}} \tag{11}$$

with an effective reaction rate k_p defined as for the liquid:

$$\frac{1}{k_p} = \frac{1}{k_{\mathrm{pyC}}} + \frac{h_p - e}{\mathcal{D}_g} \,. \tag{12}$$

In order to close the model we must specify :

- an initial condition, here uniform in space:

$$C_{\mathrm{O_2}}(t=0) = C^e_{\mathrm{O_2}} \,, \tag{13}$$

- a boundary condition at $\partial\Omega_{\mathrm{ext}}$, translating exchange with the outer atmosphere through a boundary layer with thickness δ_g:

$$\mathbf{F}_{\mathrm{O_2}} \cdot \mathbf{n} = \frac{e\mathcal{D}}{\delta_g} \left(C_{\mathrm{O_2}} - C^e_{\mathrm{O_2}}\right) \,, \tag{14}$$

- a boundary condition on $\partial\Omega_{\mathrm{in}}$, here chosen equal to eq.(14), *i.e.* assuming that the outer atmosphere also enters the intra-bundle pores,

- and a boundary condition on $\partial\Omega_f$, representing the oxygen consumption by pyrocarbon oxidation:

$$\mathbf{F}_{O_2} \cdot \mathbf{n} = e_p k_p C_{O_2} \tag{15}$$

When flow occurs, the spreading of the oxide is accounted for by the following propagation equation:

$$\frac{\partial \phi_l}{\partial t} + \mathbf{u} \cdot \nabla \phi_l = 0 \tag{16}$$

in which the fluid velocity $\mathbf{u}$ appears. To be able to solve this equation, one needs to define or compute somehow the liquid velocity $\mathbf{u}$. In our modeling approach, we have considered a potential approximation for the flow, *i.e.* that there exists a function $\Phi(x, y)$ such that $\mathbf{u} = \nabla\Phi$. Indeed, the flow is very slow and fully laminar, so we can safely assume that it is irrotational. Starting from a classical 3D potential formulation in the (moving boundary) liquid domain, with mass fluxes given on the reactive boundaries, we arrive to a 2D asymptotic crack-averaged potential equation reading:

$$\nabla \cdot (h \nabla \Phi) = Q, \tag{17}$$

Where all the mass fluxes on the 3D boundaries lead to the appearance of the source term Q condensing reading:

$$Q = -\left(2V_{m,B_2O_3} - V_{m,B_xC}\right) S_{O_2} \tag{18}$$

Note that the main unknowns of the model represent now average values across the crack opening of the material concentrations (in particular oxygen), and of the flow speed computed as the gradient of the potential obtained solving (18).

3. Numerical solution of the coupled system

Overall coupled strategy

The global algorithm is schematized in figure 3. The resolution involves three blocks, one for initialization, and two solvers for elasticity and oxidation, respectively.

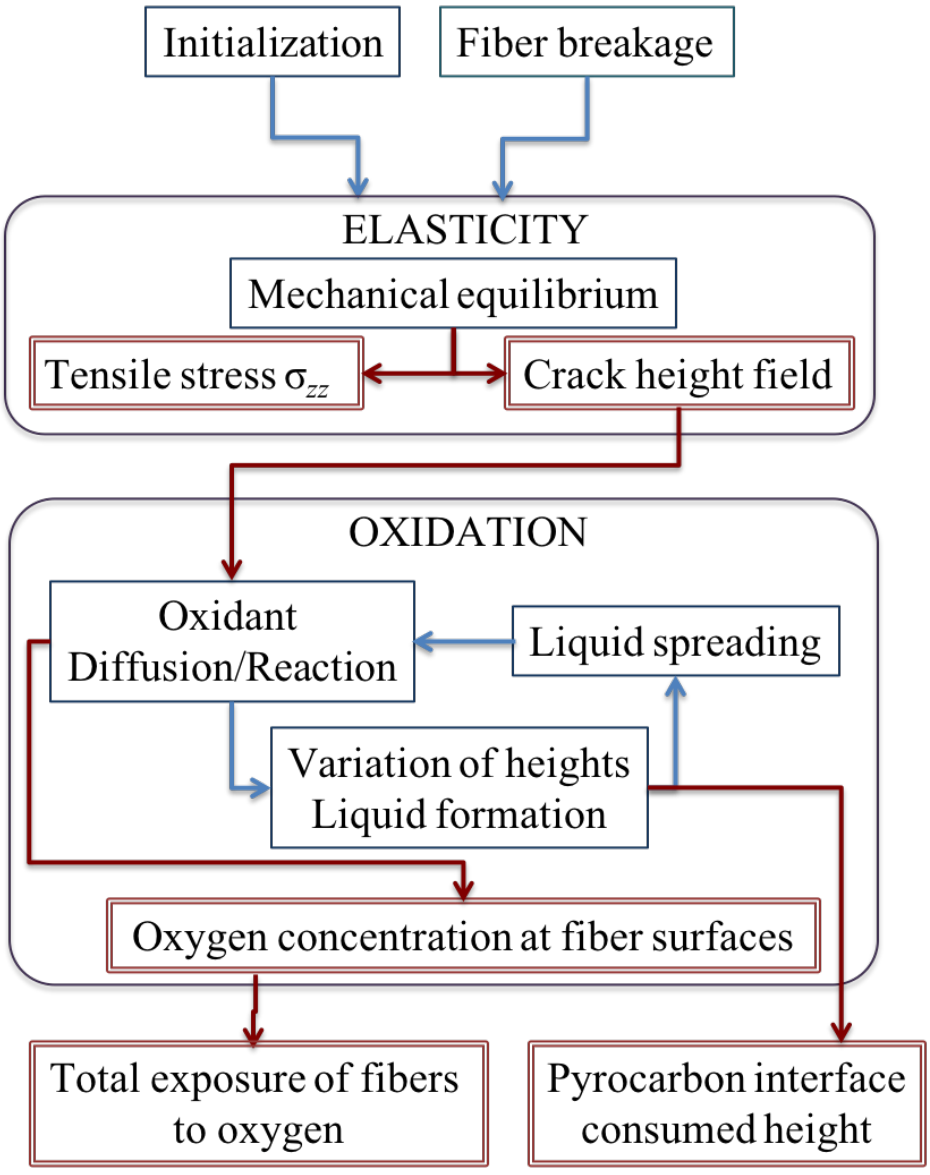

Figure 3: Overall flowchart of the resolution algorithm.

The initialization block generates two Finite Element (FE) meshes from the

initial data containing the position and diameter of all fibers, plus the different matrix (inert and reactive) layers.

The first FE solution block addresses only mechanical equilibrium by solving the elasticity equations on a 3D mesh describing the fibers, the crack in the matrix, and introducing decohesion between fibers and matrix. The crack width at every point of the matrix domain ($\Omega_i \cup \Omega_r$) is utilized in the next block.

The second block adresses oxidation and contains three subsets devoted respectively to the oxygen mass balance (diffusion and reaction, eqs. (3-7), solid and liquid mass balances (8-12)), and liquid flow (eqs. (16-**??**). The solution is obtained by chaining to each other the three subsets sequentially. The same 2D mesh is used for the solution of the three subsets. The crack width field is necessary for this block and is recovered from the first block. The output of the second block contains, among others, the total exposure of the fibers to oxygen – which is given as a criterion for life duration of the material.

Additionally, it is possible to restart the computation of the second block after a fiber breakage event. In this case, the crack is reopened and the oxygen diffusion and oxide production resume. The area corresponding to the former fiber is now integrated in the domain Ω_i (inert), but the former fiber boundary $\partial\Omega_f$ has still a reactive character, so that there is an "internal boundary" condition there :

$$[\mathbf{F}_{\mathrm{O}_2}] \cdot \mathbf{n} = e_p k_p C_{\mathrm{O}_2} \tag{19}$$

where the brackets denote the flux discontinuity between exterior and interior sides of the boundary.

3.1. Mesh generation

The starting point for the problem resolution is a 2D image, containing the fibers described by discs; their size distribution and space correlation function are

retrieved from the analysis of transverse optical micrographs of a minicomposite or of a bundle inside a composite. Once the fibers are located, the multi-layer matrix is generated by geometric dilation, either homogeneous or biased with a lesser dilation factor in the bundle center. Output of matrix image analysis or of CVI modeling is also a possible alternative as a starting point.

Two meshes are generated : the first is a fine 2D mesh for the oxidation and liquid spreading part ; the second one is a coarser 2D mesh of the same image, extruded in the third direction, in order to perform elasticity computations. A fiber/matrix decohesion can be introduced over a given length l_d.

3.2. Space and time discretization

The species mass balances are discretized using a specifically developed finite element scheme. Eqs. (3,7) are written in weak (integral) formulation, then the Green-Ostrogradski formula is applied and the boundary conditions (14-15) are inserted; the result is discretized over a basis function set and transformed into a linear algebraic system, the unknowns of which are the basis function parameters, chosen for convenience as the variable values at the integration points of the elements. Triangular P1 elements were chosen in this study.

The solution of the fluid spreading equations (eqs. (16) and (**??**) or (17)) is achieved with an inexpensive approximate numerical scheme, consisting in distributing uniformly the amount of fluid created in any connected component of the liquid phase (a"droplet") during a time increment Δt on all neighboring nodes surrounding the existing droplet. The continuity equation (**??**) in its integral form can be written as a mass balance over Δt:

$$\Delta t \int_{\partial\Omega_d/\Omega_f} h\mathbf{u}\cdot\mathbf{n}dS = \Delta t \int_{\Omega_d\cap\Omega_r} QdV \tag{20}$$

The droplet Ω_d is discretized over triangles T with faces f. Accordingly, eq; (20) can be rewritten as:

$$\Delta t \sum_{f \in \partial\Omega_d \setminus \Omega_f} h\mathbf{u} \cdot \mathbf{n} \, |f| = \Delta t \sum_{T \in \Omega_d \cap \Omega_r} Q(T) \frac{|T|}{3} \tag{21}$$

where $|f|$ and $|T|$ are the measures of the face f (length) and triangle T (area).

By analogy with this last equation, one can write :

$$\Delta t \sum_{f \in \partial\Omega_d \setminus \Omega_f} h\mathbf{u} \cdot \mathbf{n} \, |f| = \sum_{i \in \Omega_{nd} \setminus \Omega_f} (\Delta h_l)_i \frac{\left|T_{fi}\right|}{3} \tag{22}$$

where Ω_{nd} designs the set of nodes i lying outside the droplet but forming a triangle T_{fi} with a face f of the droplet boundary $\partial\Omega_d$ (see figure 4).

The height increase $(\Delta h_l)_i$ on the i^{th} mesh node neighboring the face f and lying outside of the droplet will be:

$$(\Delta h_l)_i = \Delta t \times \frac{h\mathbf{u} \cdot \mathbf{n} \, |f|}{\sum_{j \in [1; N_{nt,i}]} \left|T_j\right|} \tag{23}$$

where $N_{nt,i}$ is the number of triangles having node i as one summit, as illustrated in figure 4.

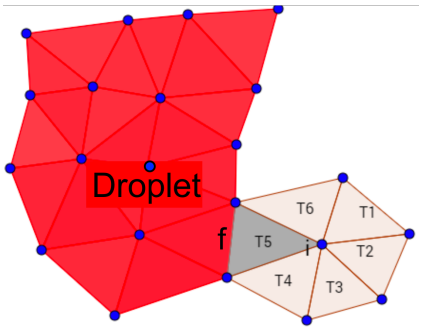

Figure 4: Scheme of a growing droplet.

The time discretization of eq. (3) follows a first-order implicit Euler scheme, which is simple but robust. The time integration of the ODEs (9-12) describing the evolution of the height variables has been achieved with a Newton-Raphson

scheme. For sake of convenience, the inverses of the heights have been chosen as the variables; an arbitrarily large value is chosen for the initialization.

The choice of the time step is rather difficult to address because of the existence of two largely different time scales in the liquid and the gas phases ($\Delta t_l = \frac{L^2}{D_l}$ and $\Delta t_g = \frac{L^2}{D_g}$, respectively, where L is the characteristic width of the crack) arising from the ratio $\frac{D_g}{D_l} \approx 10^5$ between the diffusion coefficients in both phases. Choosing a time step linked to gas diffusion t_g would lead to extremely slow computations. In a first attempt, it had been chosen to consider the diffusion equation (3) as steady, while the time integration would only rely on eqs. (9-12) [32] but after the creation of a liquid domain ($h_g = 0$) this is not possible any more. So, here, the initial time step has been set to the geometrical average of both time scales:

$$\Delta t = \sqrt{\Delta t_l \Delta t_g} \tag{24}$$

and then, after the healing event occurs, the time step is set to Δt_l. Fig 5 shows that the choice of time step (eq. (24) allows having a solution within 5% accuracy with respect to the finest time step, with a $\approx 40\times$ solution time acceleration; doubling this time step still preserves a good quality of the results, even though the precision of the implicit Newton scheme does not guarantee it in principle.

The mechanical equilibrium equations are solved by a classical finite element scheme over P1 tetrahedral elements; the matrix solution makes use of the MUMPS linear algebra library [34].

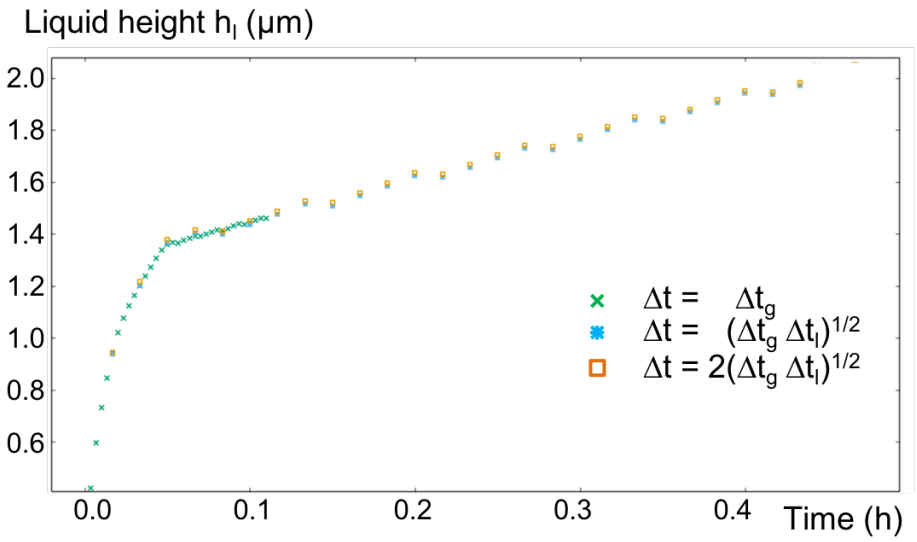

Figure 5: Time step acceleration: time evolution of the liquid height at point 2 (see fig. 6a) for several choices of the time step.

4. A numerical example

We will now present and discuss in detail an example, in order to illustrate the capabilities of the modeling framework developed. First, the construction of the resolution domain is addressed; then, all physico-chemical parameters will be given. Finally, the results will be displayed and discussed.

4.1. Problem statement

The 2D resolution domain, illustrated in Fig. 6a) is representative of a small minicomposite, with 59 fibers, the sizes and positions of which have been extracted from a transverse micrograph of an actual composite. check & elaborate - Guillaume. The multilayer matrix is generated by successive object dilations; hence, it is constituted by concentric layers around each fiber.

Then, by a simple mesh extrusion technique, a 3D mesh is produced to fully represent a segment of the minicomposite, containing the crack in its middle part,

as illustrated in Fig. 6b). Note that, as compared to the 2D mesh of the crack plane, the 2D element density is lower, and all matrix layers have been considered as having the same mechanical properties, so they are meshed in 3D as a single matrix phase (grey domain in the figure).

4.2. Geometrical and physico-chemical parameters

All the parameters of the virtual material have been chosen as representative of a realistic situation, such as the ones analyzed in previous reports [26].

We report in particular the geometrical parameters characterizing the crack simulated on table (1), while the parameters related to physics and chemistry are listed in table (2).

The oxygen/air gas diffusion coefficient has been evaluated thanks to the classical Chapman-Enskog relationship [35]. The oxygen/boria liquid diffusion coefficient and the boron carbide linear oxidation rate constant have been evaluated from experimental data on B_xC oxidation [36].

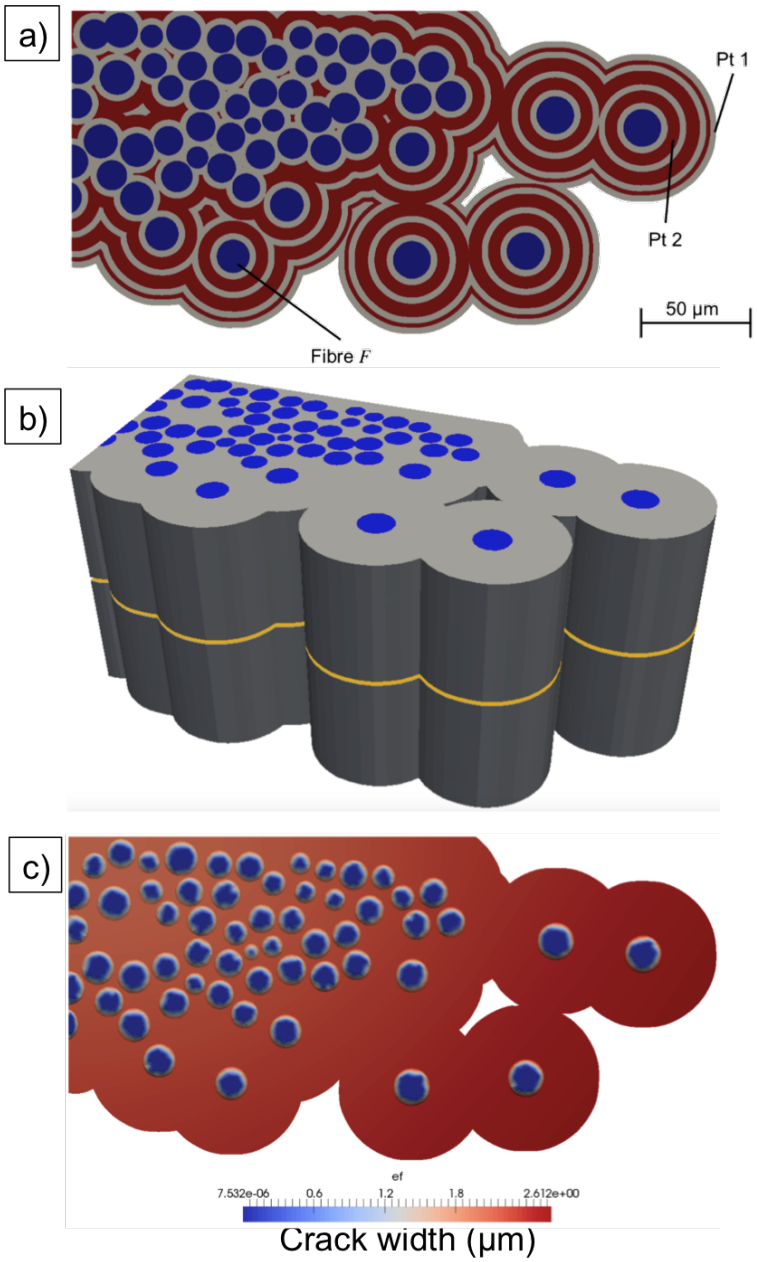

Figure 6: Description of the geometry of the example problem. a) Localization of the phases (the dark blue disks are the fibers sections, the concentric rings are respectively the sealing matrix in dark red and the inert matrix in light grey). b) 3D view of the domain used for mechanical equilibrium computations, showing the location of the crack at mid-height. c) Spatial distribution of the crack width at initial state.

Parameter	symbol	value	unit
Outer inert layer thickness		3.0	μm
Outer healing layer thickness		2.0	μm
Second inert layer thickness		3.0	μm
Second healing layer thickness		6.0	μm
Third inert layer thickness		3.0	μm
Third healing layer thickness		6.0	μm
Inner inert layer thickness		3.0	μm
Pyrocarbon thickness	e_p	0.1	μm
Average fiber diameter	$\langle d_f \rangle$	13.3	μm
Fiber diameter std. deviation	$\sigma(d_f)$	2.2	μm
Fiber volume fraction	Φ_f	48.6	%
Minicomposite section	S_0	0.0167	mm^2

Table 1: Input data for the example case: geometrical parameters.

Parameter	symbol	value	unit
Temperature	T	700	°C
Pressure	p	1.015	hPa
External oxygen mole fraction	x_{O_2}	0.21	-
Oxygen/air gas diffusion coefficient	$\mathcal{D}_g$	$1.67 \cdot 10^{-4}$	$m^2.s^{-1}$
Oxygen/boria liquid diffusion coefficient	$\mathcal{D}_l$	$3.75 \cdot 10^{-10}$	$m^2.s^{-1}$
External boundary layer size	δ	10^{-1}	m
Pyrocarbon oxidation rate constant	k_{pyC}	$1.7 \cdot 10^{-3}$	$m.s^{-1}$
Boron carbide oxidation rate constant	$k_{\mathrm{B_2O_3}}$	$1.0 \cdot 10^{-3}$	$m.s^{-1}$
Boria molar volume	$V_{m,\mathrm{B_2O_3}}$	$4.49 \cdot 10^{-5}$	$m^3.mol^{-1}$
Boron carbide molar volume	$V_{m,\mathrm{B}_x\mathrm{C}}$	$2.33 \cdot 10^{-5}$	$m^3.mol^{-1}$
Pyrocarbon molar volume	$V_{m,\mathrm{C}}$	$7.06 \cdot 10^{-6}$	$m^3.mol^{-1}$

Table 2: Input data for the example case : physico-chemical parameters.

4.3. Results and discussion

4.3.1. Oxygen diffusion and plug formation

The initial mechanical equilibrium computation yields a 3D displacement field, of which can be extracted a 2D crack height field projected on the crack surface. This is illustrated in Figure 6c). Once this field is obtained, the oxidation computation takes place. Figure 7 summarizes the evolution of the system during the first 5 hours of exposition. The upper graph gives the oxygen concentration at three points $pt1$, $pt2$ and $pt3$, one on the external boundary, one in the middle layer and the other close to a fiber (see also figure 6a) for a localization on the resolution domain). The inset of figure 7b) is a rendering of the concentration field at 0.05 hours (*i.e.* 3 minutes), illustrating the important oxygen concentration gradient all around the same boundaries. The evolution of the concentration at point $pt3$ illustrates well the whole physico-chemistry at work during this stage: first, a very rapid decrease is linked to the primary oxygen consumption by the pyrocarbon interphase and to a lesser extent by the boron carbide layers; after 3 minutes, the decrease eventually stops, because the glass formation has already managed to hinder partially the diffusion of gaseous oxygen through the formation of a continuous external barrier (see the bottom images of figure 7); at $t = 18$ minutes, the glass reaches the fiber and the oxygen concentration is consequently at its lowest. In the later period, up to 5 hours, this concentration gradually increases again, because of diffusion through the liquid barrier.

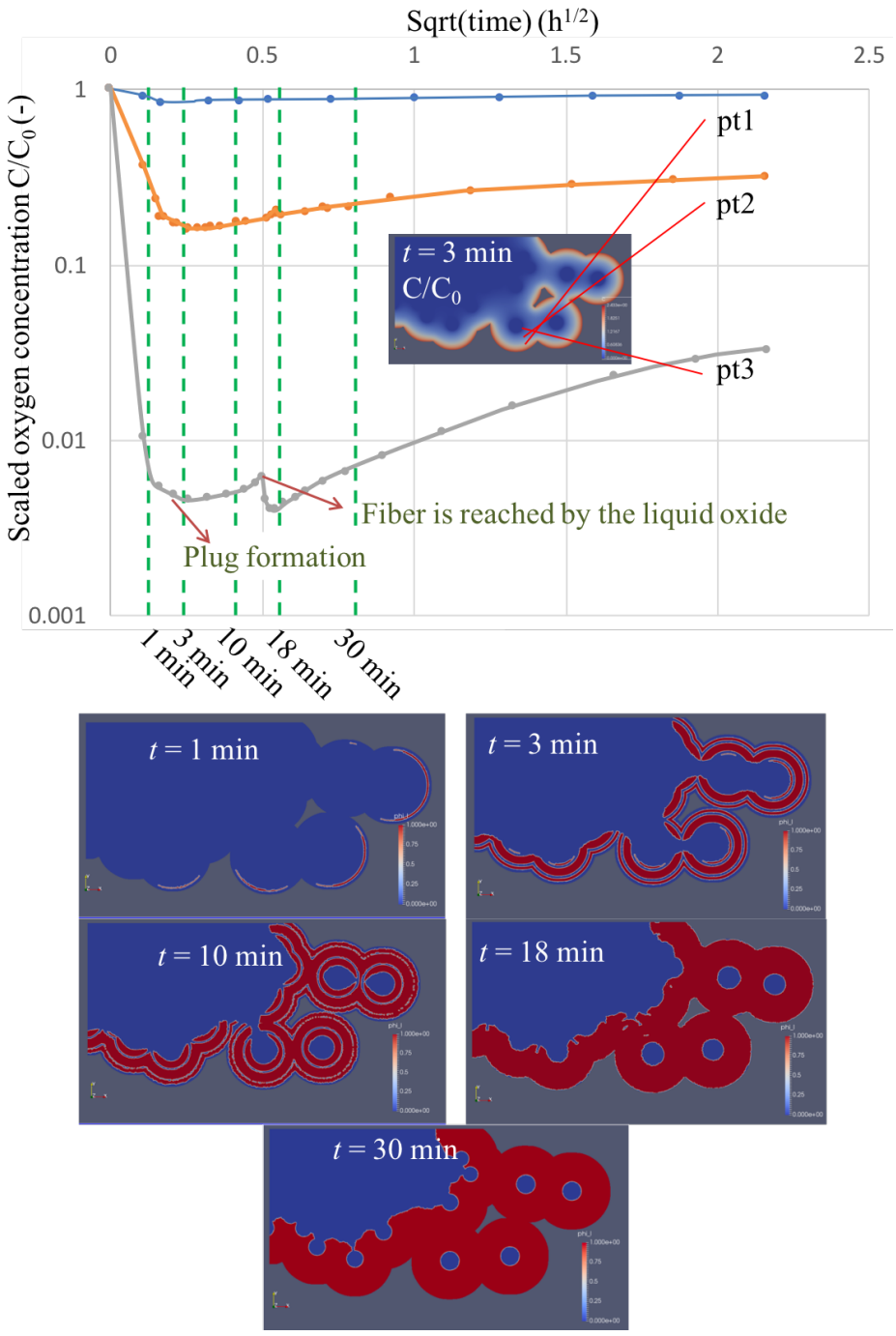

Figure 7: Effect of oxidation on the microcomposite during the first 5 hours. Top: Plot of the local oxygen concentration at selected points $pt1$, $pt2$. and $pt3$ (see figure 6a. Inset: Local oxygen concentration field at t = 3 minutes. Bottom: Extension of the liquid barrier at 5 selected moments.

Figure 8 is a map of the consumed pyrocarbon height, showing a marked gradient, not only from the outside to the interior of the mini-composite, but also on the boundary of the most external fibers, with a 1:4 ratio between the less and most exposed parts of the interphase.

Figure 8: Consumed pyrocarbon height after 30 minutes.

4.3.2. After a fiber breakage event : crack re-opening and re-healing

To illustrate the coupling capabilities of the software, a fiber breakage event has been introduced at 22 minutes. The computation has been resumed indicated above, *i.e.* considering the fiber interior as an inert, wettable domain, and letting the pyrocarbon interphase proceed reacting. Figure 9 shows that after less than 7 minutes, the broken fiber has been fully invaded by the liquid. Figure 10 is a map of the liquid height at 29 minutes (end of the computation). This quantity is equal to the crack width in all inert domains, is superior to it in all reactive domains, with a marked gradient from the exterior (larger height) to the interior (smaller height); the zones in which the liquid barrier does not yet fill the crack completely are visible in the interior of the mini-composite section.

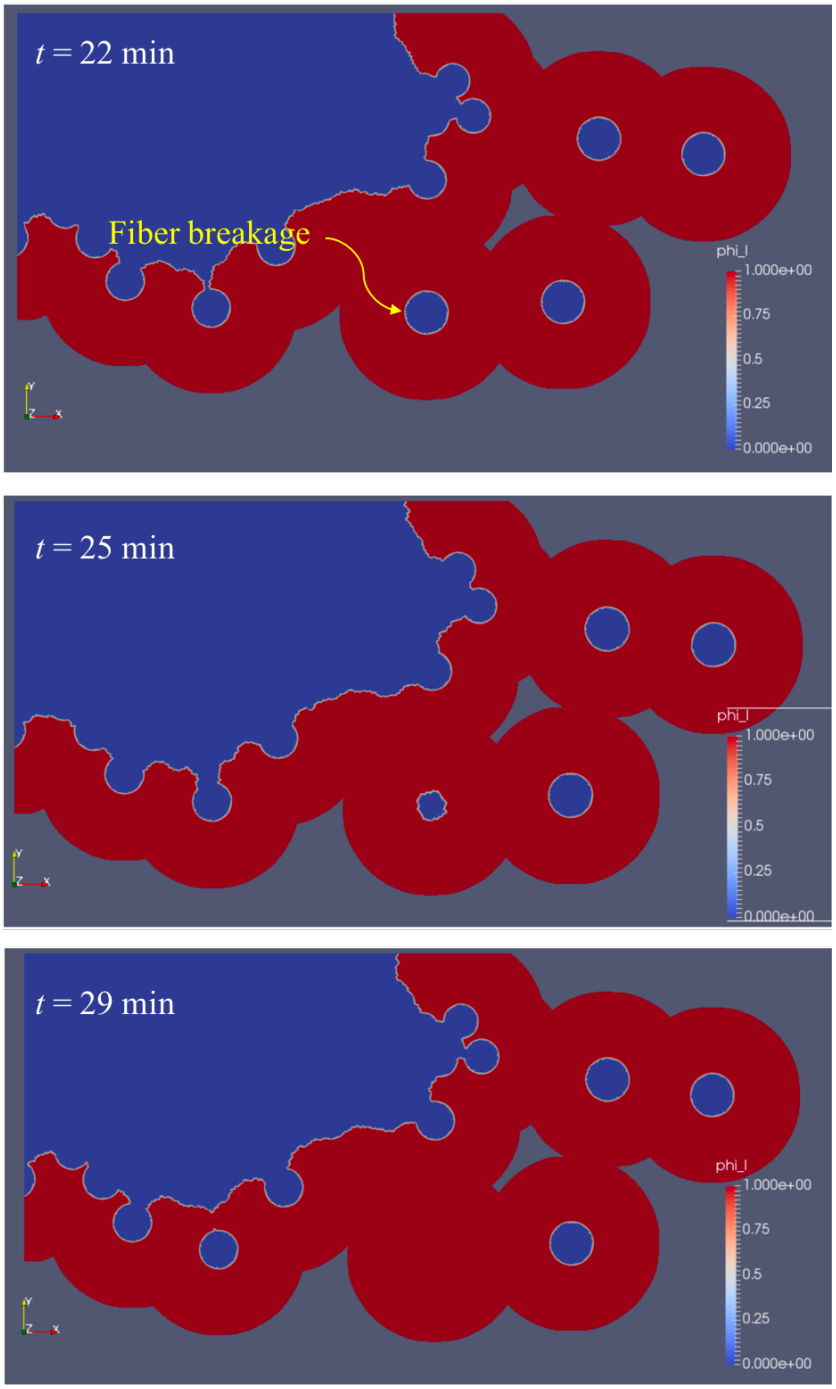

Figure 9: Evolution of the liquid barrier after a fiber breakage event.

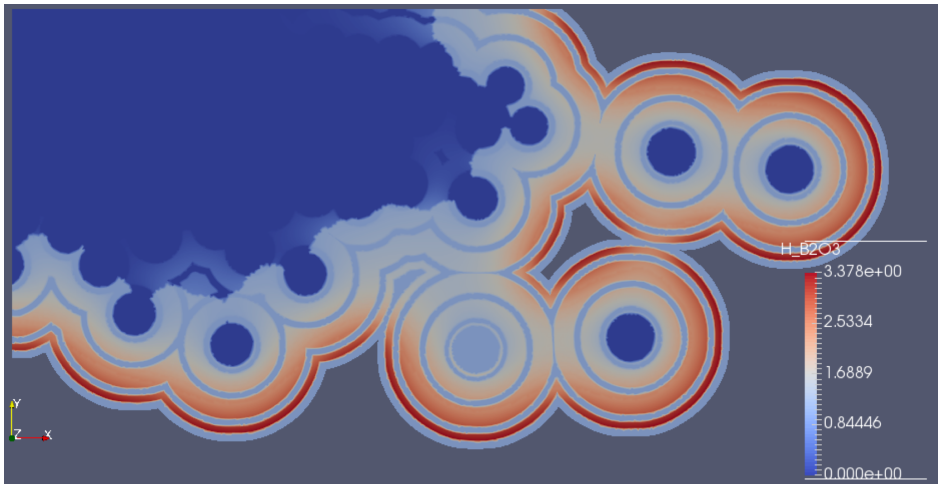

Figure 10: Liquid height after the fiber breakage event, at $t = 29$ minutes.

5. Conclusion

A detailed modeling of the behavior of self-healing Ceramic-Matrix Composite has been developed at the scale of a unidirectional bundle. This image-based model takes precisely into account the inner structure of the composite. A series of original numerical tools has been chained in a general algorithm able to describe the progressive creation of the healing fluid, even after a fiber breakage event. A realistic application example has been shown and discussed. New insights can be obtained on the interplay of the mechanical and physico-chemical mechanisms at work in the material during its life in use. Many further work directions can be defined from this point. First, varying conditions would allow having a more precise view of the influence of every phenomenon. Second, coupling the current model to a fiber subcritical crack growth model [8, 9] would allow simulating the material degradation and lifetime, and determining the most critical conditions for the composite life duration. Another improvement to the model is the incorporation of the influence of water vapor, which has the effect of partly volatilizing the boron

oxide and reducing the efficiency of the self-healing mechanism[28, 36]. Finally, the approach may be extended to other types of CMCs, with different phases, like silicon-infiltrated SiC_f/SiC composites [37].

Acknowledgement

This work has been supported by the French Ministry of Higher Education through a Ph. D. grant to G. P. and by ANR (project ViSCAP ANR-17-CE08-0030). Interns C. Boned and L. Halé are acknowledged for their help in coding. Helpful discussion with F. Rebillat (LCTS, University of Bordeaux) is gratefully acknowledged.

References

[1] F. Christin, A global approach to fiber *nD* architectures and self-sealing matrices: from research to production, Int. J. Appl. Ceram. Technol. 2 (2005) 97.

[2] J. C. Cavalier, I. Berdoyes, E. Bouillon, Composites in aerospace industry, Adv. Sci. Technol. 50 (2006) 153–162.

[3] G. Camus, Modelling of the mechanical behavior and damage processes of fibrous ceramic matrix composites: application to a 2-d sic/sic, International Journal of Solids and Structures 37 (6) (2000) 919 – 942.

[4] S. Goujard, J.-L. Charvet, J.-L. Leluan, F. Abbé, G. Lamazouade, Matériau composite protégé contre l'oxydation par une matrice autocicatrisante et son procédé de fabrication (composite material protected from oxidation by a self-healing matrix, and method for making same), French Patent No. FR95 03606 (1995).

[5] P. Forio, J. Lamon, Fatigue behaviour at high temperature in air of a 2d sic/si-b-c composite with a self-healing multilayered matrix, Ceramic Transactions 128 (2001) 127–141.

[6] L. Quémard, F. Rebillat, A. Guette, H. Tawil, C. Louchet-Pouillerie, Self-healing mechanisms of a *SiC* fiber reinforced multilayered ceramic matrix, J. Eur. Ceram. Soc. 27 (4) (2007) 2085–2094.

[7] W. Gauthier, J. Lamon, R. Pailler, Fatigue statique de monofilaments et de fils sic hi-nicalon à 500 °c et 800 °c, Revue des Composites et des Matériaux Avancés 16 (2) (2006) 221–241.

[8] P. Ladevèze, M. Genet, A new approach to the subcritical cracking of ceramic fibers, Composites Science and Technology 70 (11) (2010) 1575–1583.

[9] C. Cluzel, E. Baranger, P. Ladevèze, A. Mouret, Mechanical behaviour and lifetime modelling of self-healing ceramic-matrix composites subjected to thermomechanical loading in air, Composites Part A: Applied Science and Manufacturing 40 (8) (2009) 976–984.

[10] L. Marcin, E. Baranger, P. Ladevèze, M. Genet, L. Baroumes, Prediction of the lifetime of self-healing ceramic matrix composites: applications to structural computations, in: W. Krenkel, J. Lamon (Eds.), Procs 7^{th} International Conference on High Temperature Ceramic Matrix Composites (HT-CMC7), Univ. Bayreuth / AVISO Verlag, Berlin, 2010, pp. 194–202.

[11] F. Rebillat, Original 1d oxidation modeling of composites with complex architectures, in: M. Singh (Ed.), Procs. 5^{th} Conf. on High Temperature Ceramic Matrix Composites (HT-CMC 5), 2005, pp. 315–320.

[12] J. Lamon, A micromechanics-based approach to the mechanical behavior of brittle-matrix composites 61 (2001) 2259–2272.

[13] V. Drean, M. Ricchiuto, G. Vignoles, Two-dimensional oxydation modelling of MAC composite materials, Research Report RR-7417, INRIA (2010).

[14] F. Lamouroux, G. Camus, J. Thébault, Kinetics and mechanisms of oxidation of 2d woven c/sic composites: I, experimental approach, Journal of the American Ceramic Society 77 (8) (1994) 2049–2057.

[15] R. Naslain, F. Langlais, Fundamental and practical aspects of the chemical vapor infiltration of porous substrates, High Temperature Science 27 (1989)

221–235, 6^{th} Intl. Conf. on High TemperatureChemistry of Inorganic Materials.NIST, Gaithersburg, MD, Apr. 03-07, 1989.

[16] T. M. Besmann, B. W. Sheldon, R. A. Lowden, D. P. Stinton, Vapor-phase fabrication and properties of continuous-filament ceramic composites, Science 253 (1991) 1104–1109.

[17] G. L. Vignoles, Modelling of the CVI processes, Adv. Sci. Technol. 50 (2006) 97–106.

[18] N. Lissart, J. Lamon, Damage and failure in ceramic matrix minicomposites: Experimental study and model, Acta Materialia 45 (3) (1997) 1025–1044, cited By 73.

[19] J. Lamon, Approach to Microstructure-Behavior Relationships for Ceramic Matrix Composites Reinforced by Continuous Fibers, John Wiley & Sons, Inc., 2014.

[20] C. Chateau, L. Gélébart, M. Bornert, J. Crépin, E. Boller, C. Sauder, W. Ludwig, In situ X-ray microtomography characterization of damage in SiC_f/SiC minicomposites, Composites Science and Technology 71 (6) (2011) 916–924,

[21] O. Caty, P. Ibarroule, M. Herbreteau, F. Rebillat, E. Maire, G. L. Vignoles, Application of X-ray computed micro-tomography to the study of damage and oxidation kinetics of thermostructural composites, Nuclear Instruments and Methods in Physics Research B 324 (2014) 113–117.

[22] P. Forio, J. Lamon, High temperature behavior of ceramic matrix composites with a self healing matrix, in: C. Bathias, H. Fukuda, K. Kemmoshi, J. Renard, H. Tsuda (Eds.), Repairing Structures using Composite Wraps:

Procs. 8^{th} Japanese/European Symposium on Composite Materials, 2003, pp. 159–170, 8^{th} Japanese/European Symposium on Composite Materials, Tokyo Univ. Sci., Tokyo, Japan, Apr 16-17, 2002.

[23] P. Forio, F. Lavaire, J. Lamon, Delayed failure at intermediate temperatures (600 °-700 °C) in air in silicon carbide multifilament tows, J. Amer. Ceram. Soc. 87 (5) (2004) 888–893.

[24] W. Gauthier, J. Lamon, Delayed failure of Hi-Nicalon and Hi-Nicalon S multifilament tows and single filaments at intermediate temperatures (500 °-800 °C), Journal of the American Ceramic Society 92 (3) (2009) 702–709.

[25] W. Gauthier, F. Pailler, J. Lamon, R. Pailler, Oxidation of silicon carbide fibers during static fatigue in air at intermediate temperatures, Journal of the American Ceramic Society 92 (9) (2009) 2067–2073.

[26] F. Rebillat, Advances in self-healing ceramic matrix composites, Woodhead Publishing Ltd, 2014, Ch. 16, pp. 369–409.

[27] S. Labruquere, X. Bourrat, R. Pailler, R. Naslain, Structure and oxidation of C/C composites: role of the interface, Carbon 39 (7) (2001) 971–984.

[28] F. Rebillat, X. Martin, E. Garitte, A. Guette, Overview on the Self-Sealing Process in the SiC_f/[Si,C,B]$_m$ Composites under Wet Atmosphere at High Temperature, in: D.Singh, D.-M. Zhu, Y.-C. Zhou, M. Singh (Eds.), Design, Development, and Applications of Engineering Ceramics and Composites, Vol. 215 of Ceramics Transactions, The American Ceramic Society, John Wiley & sons, Inc., New York, 2010, pp. 151–166.

[29] X. Martin, F. Rebillat, A. Guette, Oxidation behavior of boron carbide (B_4C) in a complex atmosphere N_2/O_2H_2O, in: E. Opila, P. Hou, T. Maruyama, B.

Pieraggi, D. Shifler, and E. Wuchina (Eds.), High temperature corrosion and materials chemistry IV, Vol. 2003 of Electrochem. Soc. Procs., 2003, pp. 339–350.

[30] R. Naslain, A. Guette, F. Rebillat, S. Le Gallet, F. Lamouroux, L. Filipuzzi, C. Louchet, Oxidation mechanisms and kinetics of SiC-matrix composites and their constituents, J. Mater. Sci. 39 (24) (2004) 7303–7316.

[31] F. Nualas, F. Rebillat, A Multi-Scale Approach of Degradation Mechanisms inside a SiC(f)/Si-B-C(m) Based Self-Healing Matrix Composite in a Dry Oxidizing Environment, Oxidation of Metals 80 (3-4, SI) (2013) 279–287.

[32] V. Drean, G. Perrot, G. Couégnat, M. Ricchiuto, G. L. Vignoles, Image-based 2D numerical modeling of oxide formation in self-healing CMCs, in: W. M. Kriven, A. L. Gyekenyesi, G. Westin, J.-Y. Wang, M. Halbig, S. Mathur (Eds.), Developments in Strategic Materials and Computational Design III, Vol. 33 of Ceramics Engineering and Science Proceedings, The American Ceramic Society, Wiley, New York, 2013, pp. 117–125.

[33] B. E. Deal, A. S. Grove, General relationship for the thermal oxidation of silicon, J. Appl. Phys. 36 (2) (1965) 3770–3778.

[34] http://mumps.enseeiht.fr/: Mumps: Multifrontal massively parallel sparse direct solver [online] (December 2018) [cited December 26, 2018].

[35] R. Reid, J. Prausnitz, B. E. Poling, The Properties of Gases and Liquids, 4th Edition, McGraw-Hill, 1987.

[36] F. Rebillat, X. Martin, A. Guette, Kinetic oxidation laws of boron carbide in dry and wet environments, in: Singh, M and Kerans, RJ and LaraCurzio, E and Naslain, R (Ed.), High temperature ceramic matrix composites 5, 2005, pp. 321–326.

[37] G. N. Morscher, N. A. Gordon, Acoustic emission and electrical resistance in SiC-based laminate ceramic composites tested under tensile loading, Journal of the European Ceramic Society 37 (13) (2017) 3861–3872.